Molecular Determinants of Substrate Specificity in Plant 5′-Methylthioadenosine Nucleosidases

Karen K. W. Siu[1,2], **Jeffrey E. Lee**[1,2], **Janice R. Sufrin**[3], **Barbara A. Moffatt**[4], **Martin McMillan**[5], **Kenneth A. Cornell**[6], **Chelsea Isom**[6], and **P. Lynne Howell**[1,2,*]

[1] Program in Molecular Structure and Function, Research Institute, Hospital for Sick Children, 555 University Avenue, Toronto, Ontario, Canada M5G 1X8

[2] Department of Biochemistry, Faculty of Medicine, University of Toronto, Medical Sciences Building, Toronto, Ontario, Canada M5S 1A8

[3] Department of Pharmacology and Therapeutics, Roswell Park Cancer Institute, Elm and Carlton Streets, Buffalo, NY 14263, USA

[4] Department of Biology, University of Waterloo, Waterloo, Ontario, Canada N2L 3G1

[5] National Synchrotron Light Source, Brookhaven National Laboratory, 75 Brookhaven Avenue, Building 725B, Upton, NY 11973-5000, USA

[6] Department of Chemistry and Biochemistry, Boise State University 1910 University Dr., Boise, Idaho 83725-1520, USA

Abstract

5′-Methylthioadenosine (MTA)/S-adenosylhomocysteine (SAH) nucleosidase (MTAN) is essential for cellular metabolism and development in many bacterial species. While the enzyme is found in plants, plant MTANs appear to select for MTA preferentially, with little or no affinity for SAH. To understand what determines substrate specificity in this enzyme, MTAN homologues from *Arabidopsis thaliana* (*At*MTAN1 and *At*MTAN2, which are referred to as *At*MTN1 and *At*MTN2 in the plant literature) have been characterized kinetically. While both homologues hydrolyze MTA with comparable kinetic parameters, only *At*MTAN2 shows activity towards SAH. *At*MTAN2 also has higher catalytic activity towards other substrate analogues with longer 5′-substituents. The structures of apo *At*MTAN1 and its complexes with the substrate- and transition-state-analogues, 5′-methylthiotubercidin and formycin A, respectively, have been determined at 2.0–1.8 Å resolution. A homology model of *At*MTAN2 was generated using the *At*MTAN1 structures. Comparison of the *At*MTAN1 and *At*MTAN2 structures reveals that only three residues in the active site differ between the two enzymes. Our analysis suggests that two of these residues, Leu181/Met168 and Phe148/Leu135 in *At*MTAN1/*At*MTAN2, likely account for the divergence in specificity of the enzymes. Comparison of the *At*MTAN1 and available *Escherichia coli* MTAN (*Ec*MTAN) structures suggests that a combination of differences in the 5′-

---

[*]Corresponding author. Program in Molecular Structure and Function, Research Institute, Hospital for Sick Children, 555 University Avenue, Toronto, Ontario, Canada M5G 1X8. howell@sickkids.ca.
Present addresses: J. E. Lee, Department of Immunology, The Scripps Research Institute, 10550 North Torrey Pines Road, La Jolla, CA, 92037, USA; M. McMillan, BairdPayne Global Pharmaceutical Services, Inc., 14A Florence Street, East Patchogue, NY 11772-6186, USA.

alkylthio binding region and reduced conformational flexibility in the *At*MTAN1 active site likely contribute to its reduced efficiency in binding substrate analogues with longer 5′-substituents. In addition, in contrast to *Ec*MTAN, the active site of *At*MTAN1 remains solvated in its ligand-bound forms. As the apparent pK_a of an amino acid depends on its local environment, the putative catalytic acid Asp225 in *At*MTAN1 may not be protonated at physiological pH and this suggests the transition state of *At*MTAN1, like human MTA phosphorylase and *Streptococcus pneumoniae* MTAN, may be different from that found in *Ec*MTAN.

Keywords

conformational flexibility; 5′-methylthioadenosine/S-adenosylhomocysteine nucleosidase; 5′-methylthioadenosine; S-adenosylhomocysteine; methionine recycling

Introduction

Methionine-recycling pathways have evolved in eukaryotes and most bacterial species because the amino acid is often limited in bioavailability and is energetically costly to synthesize *de novo*.[1,2] Methionine is essential for cellular metabolism and development, and accretion of the nucleoside metabolites, 5′-methylthioadenosine (MTA) and *S*-adenosylhomocysteine (SAH) (Fig. 1), negatively regulates transmethylation reactions and quorum sensing, and polyamine biosynthesis, respectively.[3,4] In mammals, MTA is converted to 5-methylthioribose 1-phosphate (MTR 1-P) and adenine by MTA phosphorylase (MTAP),[5] while SAH is metabolized to homocysteine and adenosine by SAH hydrolase. MTAP is not found in plants and many bacterial species. In its place, MTA nucleosidase (MTAN) is used to hydrolyze MTA, and in some cases SAH. MTAN catalyzes the irreversible cleavage of the N-glycosidic bond of MTA and SAH to form adenine, and methylthioribose (MTR) and S-ribosylhomocysteine (SRH), respectively.[6–10] Adenine enters the nucleotide biosynthetic pathway, while MTR, depending on the species, is either excreted or phosphorylated at the C1-hydroxyl by MTR kinase to form MTR 1-P. MTR 1-P is subsequently isomerized to 5-methylthioribulose 1-phosphate by MTR 1-P epimerase.[11] The ensuing downstream steps in the methionine recycling pathway appear to vary somewhat between species, depending largely on whether the environment is aerobic or anaerobic, and this has been reviewed in detail by Sekowska *et al.*[11] The last step is common to all species and involves an amino group transfer from a number of potential amino acid donors to 2-keto-4-methylthiobutyrate to form methionine.[11]

While bacterial MTANs show dual-substrate specificity for both MTA and SAH, plant MTANs (typically referred to in the plant literature as MTN) exhibit a distinct preference for MTA with little or no activity towards SAH.[12–14] Like mammals, plants appear to utilize SAH hydrolase to metabolize SAH.[15,16] In addition, the methionine-recycling pathway in plants is conjugated to ethylene synthesis.[17] In the first step of ethylene synthesis, 1-aminocyclopropane-1-carboxylate (ACC) is produced from *S*-adenosylmethionine (AdoMet) with MTA released as a side product.[18] Accumulation of MTA inhibits ethylene production.[17,19] Regulation of the methionine recycling pathway by ethylene is observed in plants that synthesize high levels of ethylene for prolonged periods.[17] These include plants with

seasonal fruit ripening, such as tomatoes, and those that are submerged in water for extended periods, such as rice. In these species, MTAN is suggested to be important in seed germination and fruit ripening.[16]

The metabolic variation between the bacterial and plant MTAN's suggests structural differences that affect substrate recognition and binding. The structures and mutational analysis of a representative bacterial MTAN, *Escherichia coli* MTAN (*Ec*MTAN), have identified the catalytic residues,[20–22] and kinetic isotope effect studies[23] support the proposed S_N1-type catalytic mechanism, which is thought to begin with the donation of a proton from the catalytic acid (Asp197) to N_7 of the substrate. The protonated adenine base withdraws electrons from the ribose group, leading to elongation of the ribosidic bond and the development of a partial positive charge on the ribose group that is stabilized by the catalytic water molecule (WAT) and Glu174. Glu12 abstracts a proton from the catalytic water molecule, which then attacks $C_{1'}$ of the oxocarbenium-like intermediate to form the products.

In contrast, structural and kinetic studies on the plant enzyme(s) are more limited. The first structure of a representative plant MTAN from *Arabidopsis thaliana* (*At*MTAN1) was determined recently in complex with the product, adenine (PDB code 2H8G).[24] To better understand the mechanisms of substrate-recognition and catalysis, we have examined the substrate specificities and activity of the two MTAN homologues present in *A. thaliana*, and have determined the structure of *At*MTAN1 in its apo form, and in complex with the substrate-analogue, 5′-methylthiotubercidin (MTT), and the transition-state analogue, formycin A (FMA) (Fig. 1). A structural homology model of *At*MTAN2 has been constructed, which highlights differences in the active sites of the two isozymes that are likely critical for the substrate specificity observed. Analysis of the ligand-bound structures of *Ec*MTAN and *At*MTAN1 further suggest that differences in the dynamics, size and specificity of the active sites may account for the divergence in substrate selectivity between the bacterial and plant enzymes.

Results and Discussion

Catalytic activity and substrate specificity of AtMTAN1 and AtMTAN2

In preparation for kinetic analysis of *At*MTAN1 and *At*MTAN2 enzymes, the optimal pH and buffer conditions for activity were examined. Distinct pH optima were apparent for the two homologues (Fig. 2a). The optimal pH for *At*MTAN1 is 8, while *At*MTAN2 functions best at pH 6. When the activity was assayed at pH 7, the choice of buffer also influenced the activity (Fig. 2b). Imidazole buffer is clearly the best buffer for both enzymes. Phosphate and Hepes buffers have been commonly used in MTAN assays, but result in enzyme velocities that are only 50–60% of those found for imidazole. As observed previously for *Ec*MTAN and the closely related MTA phosphorylase and purine nucleoside phosphorylase enzymes,[10,25] Tris buffer appears to severely inhibit the nucleosidase reactions.

The kinetic parameters for *At*MTAN1 and *At*MTAN2 are summarized in Table 1. Under optimal conditions, the catalytic rate constant for *At*MTAN1 (18.7 s^{-1}) is approximately nine times greater than that found for *At*MTAN2 (2.0 s^{-1}), and shows a fourfold greater

efficiency for catabolizing MTA than AtMTAN2 (2.6 s^{-1}μM^{-1} *versus* 0.6 s^{-1}μM^{-1}). Overall, the K_m values for MTA for *A. thaliana* are similar to the values reported for MTANs from *Oryza sativa* (2.1 μM), *Lupinus luteus* (0.41 μM), *E. coli* (0.84 μM) and *Borrelia burgdorferi* (1.2 μM).[14,16,22,26] While AtMTAN1, like *L. luteus* MTAN,[16] shows no activity towards SAH, AtMTAN2 hydrolyzes SAH at 14% of the relative rate shown for MTA. This compares favorably with the *O. sativa* MTAN that is able to hydrolyze SAH at a maximum activity of 16% relative to MTA.[14]

The specificities of AtMTAN1 and AtMTAN2 for substrate analogues with different 5′-substituents have been examined, and both homologues were found to metabolize a range of nucleoside analogues. Compared to AtMTAN2, AtMTAN1 shows a sharper decrease in relative activity toward analogues with increasing 5′-alkylthio length, but maintains overall comparable levels of specific activity towards these ligands (Table 1). Additional differences are seen in the ability to catabolize adenosine and its 5′-halogenated analogues. AtMTAN1 shows no activity toward adenosine, is only weakly active against 5′-chloroadenosine (4%), and hydrolyzes 5′-iodoadenosine at a rate (28%) that is comparable to those shown for short-chain alkylthio analogues. In contrast, AtMTAN2 hydrolyzes adenosine at measurable rates (6% relative to MTA) and 5′-chloro- and iodoadenosine compounds at rates that are similar to those seen with SAH (13–17%). The lack of, or dramatically reduced activity towards adenosine may be explained by the reduced electronegativity of $O_{5'}$, which likely affects polarization of the 3′-hydroxyl group. In comparison the chloro- and iodo-substitutions may facilitate polarization of the 3′-hydroxyl group and hence residual activity is maintained. Overall, the structure–activity results suggest that AtMTAN1 is more catalytically active, but shows a narrower specificity for MTA; whereas AtMTAN2 is less active toward MTA, but more readily accommodates a wide range of 5′-substitutions on the nucleoside. The structural and modeling studies, described below, provide a rationale for the differences observed between the two enzymes.

Unlike plant MTANs, *E. coli* MTAN has comparable catalytic efficiencies for hydrolyzing MTA and SAH, with turnover numbers of 3.00±0.14 s^{-1} and 2.64±0.12 s^{-1} for MTA and SAH, respectively.[22] The specificity of EcMTAN towards MTA and SAH are also very similar, with k_{cat}/K_m values differing by less than 1.5 s^{-1}μM^{-1}.[22] The hydrolytic activity of EcMTAN towards the 5′ alkylthio-analogues 5′-ethylthioadenosine, 5′-isobutylthioadenosine and 5′-butylthioadenosine relative to MTA are 118%, 52% and 40%, respectively,[7,27] underscoring an activity profile that more closely resembles that of AtMTAN2.

Before using the substrate and transition state analogues MTT and FMA, respectively, in our structural studies, we determined whether they could inhibit the AtMTAN1 enzyme. Our results show that these compounds inhibit AtMTAN1 with K_i values of 8.3±1.2 μM and 48±5.0 μM, respectively. The affinity of AtMTAN1 for FMA is five times lower, and the affinity of MTT is ten times lower than that observed for *E. coli* MTAN. The K_i values for FMA and MTT for EcMTAN are 10 μM and 0.75 μM, respectively.[10]

The overall structure of *At*MTAN1

The structures of *At*MTAN1 in its apo form and in complex with FMA and MTT have been determined to a resolution of 2.0 Å, 1.9 Å and 1.8 Å, respectively. Electron density is not observed for the first 20, 19 and 21 residues in apo-*At*MTAN1, *At*MTAN1-FMA and *At*MTAN1-MTT, respectively; as a consequence, these residues have not been modeled in the structures. Due to the quality of the electron density observed, only the main-chain atoms have been modeled for the following side chains: apo-*At*MTAN1, Arg24B; *At*MTAN1-FMA, Ser20A, Leu23B, and Leu24B; and *At*MTAN1-MTT, Arg24A, Arg24B, Lys166A, Lys231A, Lys231B, and Glu235A; where A and B correspond to one of the two monomers in the asymmetric unit. The data collection and refinement statistics are summarized in Tables 2 and 3, respectively. The monomer of *A. thaliana* MTAN1 has a mixed α/β structure composed of a twisted, ten-stranded mixed β sheet flanked by seven α helices and two short 3_{10} helices (Fig. 3a). In the *At*MTAN1 crystals, the asymmetric unit contains two monomers, which interact *via* an interface involving the four loops β2–β3, β4–α2, β6–α2_b and β8–α4, and the α2, α2_b, and α5 helices (Fig. 3b). Detailed analysis shows that the active site of monomer A in all three structures is involved in crystallographic contacts with a neighboring subunit. No crystal contacts are observed for the active site of monomer B and, therefore, only monomer B of each structure was used in the structural analysis.

The active site of *At*MTAN1

Apo-*At*MTAN1 is the first completely ligand-free MTAN structure determined to date. Only water molecules are present in the active site (Fig. 4a). In monomer B of the *At*MTAN1-FMA and *At*MTAN1-MTT complexes, FMA and MTT are bound at 69% and 100% occupancy, respectively. The positions of the water molecules in the active site are super-imposable in all *At*MTAN1 structures, with the following exceptions: five water molecules in the apo-*At*MTAN1 structure are displaced when MTT and FMA bind; and the water molecule that bridges Thr233 and Asp225 in the MTT- and FMA-complexed structures is not present in the apo structure (Fig. 4a–c).

Both the MTT- and FMA-complexed *At*MTAN1 structures show that the adenine-binding site is formed by residues from β9, the β9–α5 loop, β10, the β10–α6 loop and α6, and the ribose-binding site is formed by α1, β5, the β9–α5 loop and β10. The 5′-substituents in both the FMA- and MTT-complexed structures are oriented *via* hydrophobic and van der Waals interactions by the side chains of Met35, Val90, Leu181, Met201 and Phe237, and Ile143, Ile145 and Phe148 from the neighboring monomer (Fig. 5a and b). The 5′-alkylthio tail of MTT is packed more tightly in the hydrophobic cavity compared to FMA, the 5′-tail of which is replaced by a less favorable hydroxyl group. Interactions in the ribose- and adenine-binding subsites are nearly identical in the MTT- and FMA-complexed structures, (Fig. 4b and c) with the following notable differences: The $O^{δ1}$ and $O^{δ2}$ atoms of the putative catalytic acid, Asp225, form hydrogen bonds with the N_6-amine group and N_7-amide group of FMA, respectively. In the MTT-complexed structure, $O^{δ1}$ of Asp225 maintains its hydrogen bond with the N_6-amine group, while the replacement of the N_7 nitrogen with a carbon atom results in an elongation of the distance (to 3.3 Å) between C_7 and the $O^{δ2}$ of Asp 225. Also, Thr116 forms a weak hydrogen bond to the $O_{4′}$ and a water-

mediated hydrogen bond to the 3′-hydroxyl of the ligand in the *At*MTAN1-FMA structure, but is over 3.3 Å away from MTT. In the FMA-but not the MTT-complex, the 2′-hydroxyl of the ligand forms a water-mediated hydrogen bond with Lys221.

Ligand-induced conformational changes in *At*MTAN1

Overall, the tertiary structures of apo-*At*MTAN1 and its complexes with FMA and MTT are highly similar, suggesting that ligand binding does not induce large conformational changes in *At*MTAN1. The root-mean-squared deviations (rmsds) of all backbone atoms between apo-*At*MTAN1, and the *At*MTAN1-FMA and *At*MTAN1-MTT structures are 0.34 Å and 0.42 Å, respectively, and 0.28 Å between the two complexes. Binding of MTT or FMA to *At*MTAN1 induces structural displacements of less than 1.5 Å in the active site region (Fig. 6). Movement of the β8–α4 and β10–α6 loops brings the catalytic residues closer to the ligand, while the α2$_b$ helix of the neighboring monomer moves approximately 1.5 Å towards the ligand, such that Ile145, Ile143 and Phe148 can form hydrophobic and van der Waals interactions with the 5′-tail of substrate (Fig. 7a). Together, the structural movements lead to a decrease in cavity volume from 76.5 Å^3 in apo form to 53.5 Å^3 when bound by MTT. Solvent is not excluded from the active site of ligand-bound *At*MTAN1.

The product-complexed structure of *At*MTAN1-ADE (PDB code 2H8G) represents the state of the enzyme after catalysis and the release of the product, 5-methylthioribose. This structure is nearly identical with the apo structure with an rmsd of 0.36 Å for all main-chain atoms. C^α displacements of less than 0.5 Å are observed for all of the active site residues, with the exception of Ala231 and Pro232, which are found on the solvent-exposed β10–α7 loop and have C^α displacements of 1.0 Å and 0.8 Å, respectively. Eight water molecules are found in the *At*MTAN1-Ade active site, seven of which superimpose with water molecules in the apo form of *At*MTAN1. Adenine displaces two water molecules present in the apo form of the enzyme.

Structural basis for the specificity differences observed for *At*MTAN1 and *At*MTAN2

Plant MTAN's for which the primary sequences are available (i.e., *A. thaliana, Vitis vinifera, O. sativa,* and *Brassica napus*) share sequence identity of 49–89% (Fig. 8). A multiple sequence alignment shows that residues that participate in substrate binding are well conserved across *At*MTAN1 and the MTAN homologues from *V. vinifera, O. sativa* and *B. napus.* Indeed between these species there is only one amino-acid difference as Met35 in *At*MTAN1 and the other species is replaced by threonine in *B. napus* MTAN. There is less conservation observed in the second *A. thaliana* MTAN homologue, as Ile145, Phe148 and Leu181 in *At*MTAN1are substituted in *At*MTAN2 by valine, leucine and methionine, respectively. Using our *At*MTAN1 structure as a template, we have built a homology model of *At*MTAN2, which suggests that while the replacement of Ile145 by Val (residue 132 in *At*MTAN2) should not lead to a significant structural change (Fig. 5), the substitution of Leu181 by Met (residue 168 in *At*MTAN2), which has a more extended side chain, may affect the binding of ligands at the 5′-alkylthio position. This could explain the generally lower specific activities and rate constants displayed by *At*MTAN2. The model also suggests that the replacement of Phe148 by Leu (residue 135 in *At*MTAN2) could reduce steric hindrance at the end of the 5′-alkylthio binding subsite, so that longer 5′-substituents may

be accommodated more easily in the *At*MTAN2 active site. When 5′-chloroadenosine or 5′-iodoadenosine is modeled into the active sites of *At*MTAN1 and *At*MTAN2, no steric clash is observed. The phenyl ring of Phe237/Phe224 in *At*MTAN1/2 faces towards and may potentially interact favorably with the halogen substituents.

Structural comparison of *Ec*MTAN and *At*MTAN1

The tertiary structures of *At*MTAN1 and *Ec*MTAN are comparable, with rmsds of 2.7 Å, 2.5 Å, 2.3 Å and 2.2 Å between their apo-, MTT- and FMA-bound forms, respectively. *Ec*MTAN and *At*MTAN1 both crystallize as dimers, but non-equivalent residues participate in intersubunit interactions and the associations are dissimilar. The intersubunit interface of *Ec*MTAN is highly hydrophobic and is dominated by van der Waals and hydrophobic interactions, while in *At*MTAN1, both polar and apolar residues are involved in hydrogen bond and van der Waals interactions. When only one subunit is used to superimpose the *Ec*MTAN and *At*MTAN1 structures, a rigid body rotation of ~10° is observed in the second monomer.

In the structural analysis presented below, the *At*MTAN1-MTT structure has been used to represent the complexed form of the plant enzyme. A "truly" apo structure of *Ec*MTAN is unavailable because the weak inhibitor adenine (10) is salvaged from the cytosol during purification and co-crystallizes with the enzyme. Nonetheless, the structure of the adenine–*Ec*MTAN complex (*Ec*MTAN–ADE) is thought to approximate the unbound apo state as the active site is open to solvent, the adenine is bound only loosely, and the ribose- and 5′-alkylthio-binding subsites are free of ligands. The *Ec*MTAN–ADE structure has therefore been used to represent the "apo" *Ec*MTAN structure in our comparison with the apo form of *At*MTAN1.

Reduced conformational flexibility in *At*MTAN1

Comparison of the secondary structures of *Ec*MTAN and *At*MTAN1 shows that the N-terminal 26 residues of *At*MTAN1 are absent from *Ec*MTAN (Fig. 6). The lack of electron density corresponding to the N-terminal 19–21 residues in the *At*MTAN1 structures suggests that this region is disordered. Two 3_{10} helices found at the C terminus and between β5 and β6 of *At*MTAN1 are substituted by loops in *Ec*MTAN. These residues are distant from the active site and likely do not affect catalytic function. The $\alpha 2_b$ helix of *At*MTAN1, which has a key role in binding the 5′-alkylthio moiety of substrates, is replaced by a loop in *Ec*MTAN. As an α-helix is more geometrically constrained than a loop, the $\alpha 2_b$ helix in *At*MTAN1 is probably less flexible than the corresponding region in *Ec*MTAN,[24] the consequence of which is discussed below.

When the structures of *Ec*MTAN and *At*MTAN1 are superimposed, six regions (the β2–β3, β3–β4, β10–α6 and 3_{10}–β7 ($\alpha 2_b$ in *At*MTAN1) loops, α3 and α4 helices) are found to deviate by more than 5 Å and these are highlighted in Fig. 3b. As the α3 helix and the β2–β3 and β3–β4 loops are distant from the active site, differences in these loops are not believed to affect enzymatic function. On the other hand, differences in the α4 helix appear to affect the solvent accessibility of the active site, while the β10–α6 loop and 3_{10}–β7 loop ($\alpha 2_b$ in *At*MTAN1) are involved in ligand binding. On ligand binding in *Ec*MTAN, helix α4

packs tightly against the β10–α6 region and excludes all except the catalytic water molecule from the active site, effectively creating a hydrophobic pocket. In the plant enzyme, while the equivalent catalytic water molecule (WAT333B, WAT274B and WAT275B in the apo-AtMTAN1, AtMTAN1-MTT and AtMTAN1-FMA structures, respectively; Fig. 4b and c) is found, additional water molecules are present and there appears to be a solvent channel leading to the exterior. Solvent penetration into a hydrophobic core has been suggested to elevate the effective dielectric constant from ~4 to ~12.[28] This means the pK_a of the proposed catalytic acid in EcMTAN, Asp197, is potentially different from the corresponding residue, Asp225, in AtMTAN1. If the carboxylic side chain of Asp225 in AtMTAN1 is deprotonated at physiological pH, then N_7 of MTA may not be protonated at the transition state of AtMTAN1. Instead, N_7 of the oxocarbenium ion may bear a partial negative charge and catalytic acceleration may come from depolarization or ionization of the 3′-OH group, which causes electron density to increase in the ribosyl group. Kinetic isotope effect studies have established this alternative reaction pathway in $Streptococcus$ $pneumonia$ MTAN and human MTAP.[29,30] The crystal structures of $S.$ $pneumonia$ MTAN (PDB code 1ZOS) and human MTAP (PDB code 1K27) demonstrate that, like AtMTAN1, water is not excluded from the active sites of these enzymes upon ligand binding.

The β10–α6 loop plays a key role in forming the adenine-binding pocket of the active site. This loop is two residues longer in AtMTAN1 than in EcMTAN, resulting in an enlarged adenine-binding subsite in the plant enzyme. In the EcMTAN-ADE structure, electron density is absent for residues 202–205 in the β10–α6 loop (Fig. 7c), suggesting that, in the apo form, this region is disordered and more dynamic in EcMTAN than in AtMTAN1. The program VOIDOO, which finds cavities and analyses volumes, further supports our hypothesis that the active site of apo-EcMTAN is more open to solvent than AtMTAN1, as the active site of the EcMTAN-ADE structure is detected as protein surface while the active site of apo-AtMTAN1 is detected as a cavity of measurable volume. Upon ligand-binding, residues 199–207 in EcMTAN move by ~11 Å and undergo a loop-to-helix transition (Fig. 7b).[20] By extending the α6 helix by a turn, the ligand is engulfed and residues Ser196, Asp197, Ala199, Phe151 and Phe207 are now in what is presumed to be the catalytically relevant conformation. In comparison, ligand-induced changes in the β10–α6 loop are much smaller in AtMTAN1, with the loop moving only ~1.0 Å (Fig. 7a) to correctly position Phe237 and Thr233.

Significant ligand-induced conformational changes are also observed in the 3_{10}–β7 loop of EcMTAN. The loop is contributed to the active site by the neighboring monomer and moves ~3.0 Å upon ligand binding to form a cap over the 5′-tail. The corresponding region in AtMTAN1 is helix α2$_b$, which moves only ~0.2 Å on ligand binding. A plot of the displacements in $C^α$ positions between the open and closed conformations of EcMTAN and AtMTAN1 (Fig. 6) shows that EcMTAN undergoes significantly greater conformational changes upon ligand binding than AtMTAN1. The combination of a more occluded active site in its open state and reduced ligand-induced conformational changes in the plant MTAN may affect the binding of ligands with bulkier 5′-tails, such as SAH.

Structural differences in the *Ec*MTAN and *At*MTAN active sites

Both *E. coli* and *A. thaliana* MTANs bind FMA and MTT in a high *syn*-conformation and the active sites are highly conserved, with only two amino acid differences. In *Ec*MTAN, Phe151 forms base-stacking interactions with the adenine ring of the bound ligand (Fig. 4d–g).[20] This residue is replaced by Leu (residue 181) in *At*MTAN1 and, as a consequence, the base-stacking interactions observed in the *E. coli* enzyme are lost. In addition, Ser76 in *Ec*MTAN is not conserved but is replaced in *At*MTAN1 by Thr116. In the *E. coli* ligand-bound structures, Ser76 forms hydrogen bonds with the N_8 and $O_{4'}$ atoms of FMA, and the $O_{4'}$ atom of MTT, respectively (Fig. 4e–g).[20] In contrast, Thr116 in the ligand-bound *At*MTAN1 structures forms a hydrogen bond to $O_{4'}$ but not the $N_{(8)}$ atom of FMA, and is over 3.4 Å from the $O_{4'}$ atom of MTT. Further, in all ligand-bound *Ec*MTAN structures determined to date, the catalytic base, Glu12 (Glu38 in *At*MTAN1), forms a water-mediated hydrogen bond with both the $2'$- and $3'$-hydroxyls of the ligand.[21] While an equivalent water molecule is present in the *At*MTAN1 structures (WAT333B, WAT274B and WAT275B in the apo-*At*MTAN1, *At*MTAN1-MTT, and *At*MTAN1-FMA structures, respectively) (Fig. 3b and c), this water molecule is hydrogen bonded to only the $3'$-hydroxyl group and is more than 3.6 Å away from the $2'$-hydroxyl group. Given that π–π stacking interactions between an aromatic residue and adenine contribute approximately 2 kcal/mol of binding energy,[31] and a hydrogen bond with an uncharged donor or acceptor contributes between 0.5–1.8 kcal/mol of binding energy,[32] the loss of these types of interactions in the *At*MTAN1 active site is certainly sufficient to explain the fivefold and tenfold difference in affinities for FMA and MTT, respectively, between *Ec*MTAN and *At*MTAN1.

The $5'$-alkylthio binding subsite of *Ec*MTAN and *At*MTAN is less conserved than the adenine- and ribose-binding subsites. Only three of the eight residues contributing to this part of the active site are conserved between the two species: Phe207/Phe237, Met9/Met35 and Met173/Met201 in *Ec*MTAN/*At*MTAN1. In *Ec*MTAN Ile50 and Val102 are conservatively substituted by Val90 and Ile143, respectively, while *Ec*MTAN Phe105 and Phe151 are replaced by the non-aromatic aliphatic residues, Ile145 and Leu181, respectively. More importantly, helix $\alpha 2_b$ of *At*MTAN1 is nine residues shorter than the corresponding 3_{10}–$\beta 7$ loop in *Ec*MTAN. As a consequence, there is no residue in *At*MTAN1 equivalent to Pro113 found in the 3_{10}–$\beta 7$ loop in *Ec*MTAN, and the $5'$-alkylthio binding subsite is therefore more constricted in *At*MTAN1. The decrease in size of the $5'$-alkylthio binding region contributes to the reduced overall volume of the ligand-bound *At*MTAN1 active site (53.5 Å^3) compared to *Ec*MTAN (70.0 Å^3), despite the enlarged adenine- and ribose-binding regions in the plant enzyme. In *At*MTAN1, Phe148 is located 3.9 Å and 5.0 Å away from the $5'$-alkylthio tail of MTT and FMA, respectively (Fig. 7d). The corresponding residue in *Ec*MTAN, Tyr107, is located 6.0 Å and 7.7 Å from MTT and FMA, respectively (Fig. 7d). The more constricted $5'$-alkylthio binding subsite and more rigid helix $\alpha 2_b$ in *At*MTAN1 likely contribute to the preference of the plant enzyme for ligands with smaller $5'$-substituents (Table 1). In addition, Phe148 of *At*MTAN1 cannot serve as a hydrogen bond donor to the carboxyl group at the $5'$-end of SAH. In fact, the hydrophobic aromatic side chain of Phe148 would likely repel a polar or charged group. The importance of Tyr107 for *Ec*MTAN function has been demonstrated previously by mutational analysis.[22] When Tyr107 is mutated to phenylalanine, the binding affinities for MTA and SAH are reduced by

258% and 131%, respectively, and the turnover numbers for MTA and SAH are reduced by 17% and 23%, respectively.

Biological implications

Despite the high sequence identity of 63%, the two MTAN homologues from *A. thaliana* demonstrate distinct substrate preferences and pH optima, suggesting that the two enzymes have unique roles in the methionine recycling pathway. *At*MTAN1 likely dominates MTA metabolism because it more specifically and efficiently hydrolyses MTA, and its mRNA is expressed in all tissue types through all developmental stages at levels at least ten times those found for *At*MTAN2.[33] While *At*MTAN2 can metabolize SAH (Table 1), SAH levels in plants are typically low at 1–50 μM.[34,35] As two copies of the SAH hydrolase gene are present in *A. thaliana* (At13940 and At3g23810), it may be that *At*MTAN2 is not contributing to SAH hydrolysis under normal growth conditions.

Structural analysis of the bound and unbound forms of *At*MTAN1 and *Ec*MTAN revealed differences that contribute to the divergence in substrate selectivity between bacterial and plant MTANs. Compared to the bacterial counterpart, the active site of apo-*At*MTAN1 is less open to solvent and the binding of ligands induce smaller structural changes. Also, the 3_{10}–β7 loop in *Ec*MTAN is replaced by an α helix ($\alpha2_b$) in *At*MTAN1, which is more geometrically constrained. Differences between *Ec*MTAN and *At*MTAN1 in the magnitude of ligand-induced conformational changes and secondary structures suggest that the plant active site is likely less flexible, which may contribute to its reduced efficiency in binding larger substrates. In addition, the 5′-alkylthio binding subsite is more constricted in *At*MTAN1. The reduced flexibility in the active site region and size of the 5′-alkylthio binding subsite in *At*MTAN1 likely explains its distinct substrate preference for MTA over SAH, which contains a branched and extended 5′-substitutent. Interestingly, unlike *Ec*MTAN, the active site of this plant enzyme remains solvated in ligand-bound state. This suggests that the apparent pK_a of Asp225 in *At*MTAN1may be significantly lower than that of Asp197 in *Ec*MTAN and that Asp225 may not act as a catalytic acid in the plant enzyme. Instead, like human MTAP and *S. pneumoniae* MTAN, catalytic acceleration may come from the stabilization of the transition state by polarization or ionization of the 3′-hydroxyl group.

Materials and Methods

Expression and purification of *At*MTAN1 and *At*MTAN2

The *A. thaliana* MTAN1 (At4g38800) cDNA was cloned from *A. thaliana* genomic DNA into the pET28a+ vector (Novagen) at the NdeI and HindIII sites to allow overexpression of the enzyme with a cleavable N-terminal His$_6$ tag. *At*MTAN1 (molecular mass 28,451 Da) was over-expressed in BL21 Codon+ cells by growing in Luria-Bertani broth (LB) to exponential phase and then inducing with 1 mM isopropyl thiogalactopyranoside (IPTG) for 4 h at 37 °C. The cells were harvested by centrifugation in a JA-10 rotor at 4000 rpm for 15 min. After freezing overnight at −20 °C, the cells were lyzed by suspending in BugBuster Protein Extraction Reagent (Novagen) with Complete EDTA-free Protease Inhibitor Cocktail (Roche) and vortex mixing for 20 minutes. The crude lysate was fractionated by

centrifugation at 18,000 rpm in a JA-20 rotor at 4 °C for 20 min. *At*MTAN1 was purified by passing the soluble fraction through a Ni-NTA agarose column (Qiagen) pre-equilibrated with 50 mM NaH$_2$PO$_4$ (pH 7.5), 20 mM imidazole. The column was washed with 50 mM NaH$_2$PO$_4$ (pH 7.5), 20 mM imidazole, and the enzyme was eluted from the column with 50 mM NaH$_2$PO$_4$ (pH 7.5), 68 mM imidazole; the protein was >95% pure. The protein was subsequently dialyzed overnight against 20 mM Tris–HCl (pH 8.4), 150 mM NaCl, 2.5 mM CaCl$_2$. Before removal of the N-terminal His$_6$ tag by thrombin cleavage for 1 h at room temperature, 10% (v/v) glycerol was added to the protein solution. Proteolysis was terminated by adding 1 mM phenylmethylsulfonyl fluoride (PMSF). Any uncleaved product and the His$_6$ tag were removed by passing the protein over the Ni-NTA agarose column. For crystallization, *At*MTAN1 was purified by isocratic elution with 25 mM Na-Hepes (pH 7.5) on a Superdex-200 HR 10/30 column. The purity of the samples was validated by SDS-PAGE and by electrospray ionization mass spectrometry at the Advanced Protein Technology Centre at The Hospital for Sick Children. Approximately 10 mg of pure *At*MTAN1 was obtained from 1 L of bacterial culture.

The selenomethioninyl derivative of *At*MTAN1 (Se-*At*MTAN1) was over-expressed and purified as described above, with the following modifications: (i) the protein was expressed in M9 medium supplemented with 60 μg/mL of D/L-selenomethionine, 100 μg/mL of L-Tyr, L-Phe and ^{1}-Lys, 40 μg/mL of all L-amino acids except for Met, Tyr, Phe and Lys, 0.4% (w/v) glucose, 2 mM MgSO$_4$, 25 μg/mL of FeSO$_4$.7H$_2$O, 1 μg/mL of riboflavin, 1 μg/mL of niacinamide, 1 μg/mL of pyridoxine monohydrochloride, 1 μg/mL of thiamine and 50 μg/mL of kanamycin; and (ii) 0.5 mM DTT (Sigma) was added to all purification buffers to prevent oxidation of the selenium.

The expression and purification of *At*MTAN2 (At4g34840) (molecular mass 27,462 Da) was similar to that of *At*MTAN1, with only minor alterations: (i) induced cell pellets were lyzed with Bacterial Lysis Reagent (Sigma-Aldrich Chemicals); and (ii) the recombinant enzyme eluted from Ni-NTA resin with 50 mM NaH$_2$PO$_4$ (pH 7.5), 250 mM imidazole. The amount of purified *At*MTAN2 obtained was sufficient for kinetic characterization but insufficient for crystallization trials.

Kinetic characterization of *At*MTAN1 and *At*MTAN2

Enzyme specific activity measurements were performed in triplicate at 22 °C in 1 mL reactions containing 100 μM nucleoside in 100 mM sodium phosphate buffer (pH 4, 5, 6, 7, 8 or 9), or 100 mM imidazole (pH 7) using a Varian Cary 100 spectrophotometer. The amount of enzyme used varied from 0.5–5 μg, and remained constant across all nucleosides tested in an activity series. Catalytic activity was observed as a decrease in A_{275} that corresponds to the hydrolysis of the nucleoside. Specific activities were calculated using the extinction coefficient for the hydrolysis of MTA (ε_{275}=1.6 mMs^{-1} cm^{-1}).[36] Kinetic constants were determined from similar assays performed in quadruplicate using 1–20 μM MTA and fitting the substrate–velocity plots to the Michaelis–Menton equation using Igor Pro 5.0 software. Relative catalytic activities towards the other substrates were determined using a single substrate concentration (100 μM).

The inhibitory constants of FMA (Fluka) and MTT were determined using a xanthine oxidase-coupled spectrophotometric assay.[37] For each molecule of adenine oxidized by xanthine oxidase, two molecules of 2-(4-iodophenyl)-3-(4-nitrophenyl)-5-phenyltetrazolium chloride (INT) are reduced to formazan, a colored product that absorbs at 470 nm.[38] All reactions were performed in triplicate in 50 mM Na-Hepes (pH 7.5) using 0.12 μg of AtMTAN1, 0.28 unit of xanthine oxidase (Sigma-Aldrich Chemicals) and 1 mM INT (Sigma-Aldrich Chemicals) in a final volume of 800 μl. The concentration of 5′-methylthioadenosine was varied from 1.5 μM to 190 μM. The reactions were monitored on a Biochrome Ultrospec 2100 UV/Vis spectrophotometer with the SWIFT II enzyme kinetics software (Amersham Pharmacia Biotech). Changes in absorption at 470 nm were converted to the amount of adenine released using the molar absorption coefficient of 15,400 $M^{-1}cm^{-1}$ at pH 7.0.[39] The inhibition constants of FMA and MTT were determined by adding 50 μMFMA or 5 μM MTT (final concentrations) to the reaction mixtures. Initial velocity data were used to determine the apparent K_m (K_m') by fitting the initial velocity data to the Michaelis–Menten equation using the SigmaPlot Enzyme Kinetics module, and K_i was calculated using the following equation:

$$K_m'=K_m(1+[I]/K_i)$$

Crystallization of Se-AtMTAN1-FMA, AtMTAN1, AtMTAN1-FMA and AtMTAN1-MTT

Se-AtMTAN1 and AtMTAN1 were concentrated to 10 mg/mL using Millipore BioMax 10K Ultrafree-0.5 mL centrifugal concentrators before crystallization. Se-AtMTAN1 was pre-incubated with 1 mM FMA for 1 h at room temperature and the complex was crystallized using the hanging-drop, vapor-diffusion technique by mixing 4 μL of Se-AtMTAN1-FMA with 2 μL of 70 mM $CH_3.COONa·3H_2O$, pH4.6, 5.6% (w/v) polyethylene glycol (PEG) 4000, 30% (v/v) glycerol. Crystals of Se-AtMTAN1 of approximately 0.1×0.1 mm grew within three days and were flash-frozen in a stream of liquid nitrogen gas without need for further cryoprotection. The crystals were initially characterized on our in-house X-ray diffraction equipment (Rigaku RUH3R rotating anode generator with Osmic optics and a Rigaku R-AXIS IV++ image plate) at The Hospital for Sick Children before collecting multiple anomalous diffraction data on Beam line X29 at the National Synchrotron Light Source, Brookhaven National Laboratory.

Native AtMTAN1 was crystallized in its apo form and in complex with FMA and MTT. Apo-AtMTAN1 was crystallized by mixing 4 μL of AtMTAN1 (10 mg/mL) with 2 μL of 0.2 M NH_4Cl, 20% (w/v) PEG3350. Crystals of approximately 0.15 mm×0.1 mm appeared after nine days and were soaked in 0.2 M NH_4Cl, 20% (w/v) PEG3350, 15% (v/v) ethylene glycol for 1 min before flash-freezing in a stream of liquid nitrogen gas. Co-crystals of AtMTAN1 with FMA or MTT were prepared by first incubating the protein with either 1 mM FMA or 0.5 mM MTT for 1 h at room temperature. AtMTAN1-FMA was crystallized by mixing 4 μL of AtMTAN1-FMA (10 mg/mL) with 2 μL of 0.2 M NH_4Cl, 15% (w/v) PEG3350 and was cryo-protected by soaking a crystal for 2 min in 0.2 M NH_4Cl, 20% (w/v) PEG3350, 15% (v/v) ethylene glycol before data collection. AtMTAN1-MTTwas crystallized by mixing 4 μL of AtMTAN1-MTT (10 mg/mL) with 2 μL of 0.2 M NH_4Cl,

20% (w/v) PEG3350, with 15% (v/v) ethylene glycol and did not require further cryo-protection before data collection. The diffraction data for the native *At*MTAN1 crystals were measured on our in-house X-ray diffraction equipment.

Structural determination and analysis of *At*MTAN1 structures

All diffraction data were reduced using d*TREK.[40] The Se-*At*MTAN1-FMA anomalous substructure was solved using the MAD data in SHELXD,[41] and the initial model of the protein was built using RESOLVE,[42,43] and by manual building in COOT.[44] The structures of apo-*At*MTAN1, and its complexes with FMA and MTT were subsequently solved by molecular replacement using PHASER with a monomer of the refined Se-*At*MTAN1-FMA structure as the search model.[45] Data up to 2.5 Å resolution were used in cross-rotation and translation searches. All structures were refined by iterative rounds of manual rebuilding using COOT alternated with restrained refinement using REFMAC.[46] Once R and R_{free} were below 0.3, water molecules were added manually and using ARP-wARP.[47,48] FMA and MTT were manually fit into electron density, and the coordinates were refined using the AutoLigand wizard in PHENIX,[49] and in subsequent rounds of restrained refinement. While MTT binds to both subunits of *At*MTAN1-MTT at full occupancy, the structure of *At*MTAN1-FMA shows that FMA is not bound in monomer A and is partially present with occupancy of 0.69 in monomer B. The occupancy of the molecule was refined iteratively to ensure no negative density was observed in the $2F_{\text{o}}$–F_{c} map and so that the temperature factor of the molecule was similar to those of surrounding protein residues. To compare the structures of *At*MTAN1 and *Ec*MTAN, the central β-strands of each protein were aligned by least-squares minimization of the main-chain N, C$^{\alpha}$ and C atoms using the PROFIT program written by Dr G. David Smith. Cavity detection and solvent-accessible volumes were computed using VOIDOO.[50] The homology model of *At*MTAN2 was generated using SWISS-MODEL and the structure of *At*MTAN1 as search template.[51] Default parameters were used throughout the model building process.

Primary sequence alignment

Using BLAST,[52] known and hypothetical plant MTAN sequences were retrieved from the UniProt Knowledge-base, [53] and the plant genome and plantEST database of the National Center for Biotechnology Information (NCBI). DNA sequences were first translated using the translate tool at the ExPASy proteomics server,[54] and then aligned with the available protein sequences using CLUSTALW with manual editing.[55]

Protein Data Bank accession codes

The coordinates and structure factors for apo-*At*MTAN1 and its complexes with FMA and MTT have been deposited in the PDB with accession codes 2QSU, 2QTT and 2QTG, respectively.

Acknowledgments

Abbreviations used

MTA	5′-methylthioadenosine
SAH	S-adenosylhomocysteine
***At*MTAN1**	*Arabidopsis thaliana* 5′-methylthioadenosine nucleosidase 1
***At*MTAN2**	*Arabidopsis thaliana* 5′-methylthioadenosine/*S*-adenosylhomocysteine nucleosidase 2
***Ec*MTAN**	*Escherichia coli* 5′-methylthioadenosine/*S*-adenosylhomocysteine nucleosidase
ADE	adenine
MTT	5′-methylthiotubercidin
FMA	formycin A
PDB	Protein Data Bank
MTR	5-methylthioribose
GOL	glycerol
PEG	polyethylene glycol
MME	monomethyl ether
WT	wild type
MTR 1-P	5′-methylthioribose 1-phosphate
rmsd	root-mean-squared deviation

References

1. Cooper AJ. Biochemistry of sulfur-containing amino acids. Annu Rev Biochem. 1983; 52:187–222. [PubMed: 6351723]

2. Schlenk F, Zydek-Cwick CR, Dainko JL. 5′-Methylthioadenosine and related compounds as precursors of S-adenosylmethionine in yeast. Biochim Biophys Acta. 1973; 320:357–362. [PubMed: 4796087]

3. Riscoe MK, Brouns MC, Fitchen JH. Purine metabolism as a target for leukemia chemotherapy. Blood Rev. 1989; 3:162–173. [PubMed: 2676034]

4. Sufrin JR, Meshnick SR, Spiess AJ, Garofalo-Hannan J, Pan XQ, Bacchi CJ. Methionine recycling pathways and antimalarial drug design. Antimicrob Agents Chemother. 1995; 39:2511–2515. [PubMed: 8585735]

5. Pegg AE, Williams-Ashman HG. On the role of S-adenosyl-L-methionine in the biosynthesis of spermidine by rat prostate. J Biol Chem. 1969; 244:682–693. [PubMed: 4889860]

6. Duerre JA. A hydrolytic nucleosidase acting on S-adenosylhomocysteine and on 5′-methylthioadenosine. J Biol Chem. 1962; 237:3737–3741.

7. Della Ragione F, Porcelli M, Carteni-Farina M, Zappia V, Pegg AE. Escherichia coli S-adenosylhomocysteine/5′-methylthioadenosine nucleosidase. Purification, substrate specificity and mechanism of action. Biochem J. 1985; 232:335–341. [PubMed: 3911944]

8. Zappia, V., Della Ragione, F., Carteni-Farina, M. Biological Methylation and Drug Design: Experimental and Clinical Roles of S-Adenosylmethionine. The Humana Press Inc; Clifton, NJ: 1985.

9. Shimizu S, Yamada H. Enzymatic process for the production of pharmacologically useful nucleosides. Ann NY Acad Sci. 1988; 542:423–427. [PubMed: 3228238]

10. Cornell KA, Swarts WE, Barry RD, Riscoe MK. Characterization of recombinant Eschericha coli 5′-methylthioadenosine/S-adenosylhomocysteine nucleosidase: analysis of enzymatic activity and substrate specificity. Biochem Biophys Res Commun. 1996; 228:724–732. [PubMed: 8941345]

11. Sekowska A, Denervaud V, Ashida H, Michoud K, Haas D, Yokota A, Danchin A. Bacterial variations on the methionine salvage pathway. BMC Microbiol. 2004; 4:9. [PubMed: 15102328]

12. Kushad MM, Richardson DG, Ferro AJ. 5′-Methylthioadenosine nucleosidase and 5-methy-lthioribose kinase activities and ethylene production during tomato fruit development and ripening. Plant Physiol. 1985; 79:525–529. [PubMed: 16664444]

13. Baxter C, Coscia CJ. In vitro synthesis of spermidine in the higher plant, Vinca rosea. Biochem Biophys Res Commun. 1973; 54:147–154. [PubMed: 4741562]

14. Rzewuski G, Cornell KA, Rooney L, Burstenbinder K, Wirtz M, Hell R, Sauter M. OsMTN encodes a 5′-methylthioadenosine nucleosidase that is up-regulated during submergence-induced ethylene synthesis in rice (Oryza sativa L.). J Expt Bot. 2007; 58:1505–1514.

15. Guranowski A, Pawelkiewicz J. Adeno-sylhomocysteinase from yellow lupin seeds. Purification and properties. Eur J Biochem. 1977; 80:517–523. [PubMed: 923592]

16. Guranowski AB, Chiang PK, Cantoni GL. 5′-Methylthioadenosine nucleosidase. Purification and characterization of the enzyme from Lupinus luteus seeds. Eur J Biochem. 1981; 114:293–299. [PubMed: 6783408]

17. Burstenbinder K, Rzewuski G, Wirtz M, Hell R, Sauter M. The role of methionine recycling for ethylene synthesis in Arabidopsis. Plant J. 2007; 49:238–249. [PubMed: 17144895]

18. Sauter M, Lorbiecke R, Ouyang B, Pochapsky TC, Rzewuski G. The immediate-early ethylene response gene OsARD1 encodes an acireductone dioxygenase involved in recycling of the ethylene precursor S-adenosylmethionine. Plant J. 2005; 44:718–729. [PubMed: 16297065]

19. Baur AH, Yang SF. Methionine metabolism in apple tissue in relation to ethylene biosynthesis. Phytochemistry. 1972; 11:3207–3214.

20. Lee JE, Cornell KA, Riscoe MK, Howell PL. Structure of Escherichia coli 5′-methylthioadenosine/S-adenosylhomocysteine nucleosidase inhibitor complexes provide insight into the conformational changes required for substrate binding and catalysis. J Biol Chem. 2003; 278:8761–8770. [PubMed: 12496243]

21. Lee JE, Smith GD, Horvatin C, Huang DJ, Cornell KA, Riscoe MK, Howell PL. Structural snapshots of MTA/AdoHcy nucleosidase along the reaction coordinate provide insights into enzyme and nucleoside flexibility during catalysis. J Mol Biol. 2005; 352:559–574. [PubMed: 16109423]

22. Lee JE, Luong W, Huang DJ, Cornell KA, Riscoe MK, Howell PL. Mutational analysis of a nucleosidase involved in quorum-sensing autoinducer-2 biosynthesis. Biochemistry. 2005; 44:11049–11057. [PubMed: 16101288]

23. Singh V, Lee JE, Nunez S, Howell PL, Schramm VL. Transition state structure of 5′-methylthioadenosine/S-adenosylhomocysteine nucleosidase from Escherichia coli and its similarity to transition state analogues. Biochemistry. 2005; 44:11647–11659. [PubMed: 16128565]

24. Park EY, Oh S, Nam MJ, Shin JS, Kim K, Song HK. Crystal structure of 5′-methylthioadenosine nucleosidase from Arabidopsis thaliana at 1.5-Å resolution. Proteins: Struct Funct. 2006:65.

25. Appleby TC, Mathews II, Porcelli M, Cacciapuoti G, Ealick SE. Three-dimensional structure of a hyperthermophilic 5′-deoxy-5′-methylthioadenosine phosphorylase from Sulfolobus solfataricus. J Biol Chem. 2001; 276:39232–39242. [PubMed: 11489901]

26. Parveen N, Cornell KA, Bono JL, Chamberland C, Rosa P, Leong JM. Bgp, a secreted glycosaminoglycan-binding protein of Borrelia burgdorferi strain N40, displays nucleosidase activity and is not essential for infection of immunodeficient mice. Infect Immun. 2006; 74:3016–3020. [PubMed: 16622242]

27. Ferro AJ, Barrett A, Shapiro SK. Kinetic properties and the effect of substrate analogues on 5′-methylthioadenosine nucleosidase from Escherichia coli. Biochim Biophys Acta. 1976; 438:487–494. [PubMed: 782530]

28. Dwyer JJ, Gittis AG, Karp DA, Lattman EE, Spencer DS, Stites WE, Garcia-Moreno EB. High apparent dielectric constants in the interior of a protein reflect water penetration. Biophys J. 2000; 79:1610–1620. [PubMed: 10969021]

29. Singh V, Schramm VL. Transition-state structure of human 5′-methylthioadenosine phosphorylase. J Am Chem Soc. 2006; 128:14691–14696. [PubMed: 17090056]

30. Singh V, Schramm VL. Transition-state analysis of S. pneumoniae 5′-methylthioadenosine nucleosidase. J Am Chem Soc. 2007; 129:2783–2795. [PubMed: 17298059]

31. Boehr DD, Farley AR, Wright GD, Cox JR. Analysis of the pi-pi stacking interactions between the aminoglycoside antibiotic kinase APH(3′)-IIIa and its nucleotide ligands. Chem Biol. 2002; 9:1209–1217. [PubMed: 12445771]

32. Fersht AR. Relationships between apparent binding energies measured in site-directed mutagenesis experiments and energetics of binding and catalysis. Biochemistry. 1988; 27:1577–1580. [PubMed: 3365411]

33. Zimmermann P, Hirsch-Hoffmann M, Hennig L, Gruissem W. GENEVESTIGATOR. Arabidopsis microarray database and analysis toolbox. Plant Physiol. 2004; 136:2621–2632. [PubMed: 15375207]

34. Moffatt BA, Stevens YY, Allen MS, Snider JD, Pereira LA, Todorova MI, et al. Adenosine kinase deficiency is associated with developmental abnormalities and reduced transmethylation. Plant Physiol. 2002; 128:812–821. [PubMed: 11891238]

35. Wagner KG, Backer AI. Dynamics of nucleotides in plants studied on a cellular basis. Int Rev Cytol. 1992; 134:1–84.

36. Singh V, Evans GB, Lenz DH, Mason JM, Clinch K, Mee S, et al. Femtomolar transition state analogue inhibitors of 5′-methylthioadenosine/S-adenosylhomocysteine nucleosidase from Escherichia coli. J Biol Chem. 2005; 280:18265–18273. [PubMed: 15749708]

37. Dunn S, Bryant J. A simple spectrophotometric assay for plant 5′-deoxy-5′-methylthioadenosine nucleosidase using xanthine oxidase as a coupling enzyme. Phytochem Anal. 1994; 5:286–293.

38. de Groot H, de Groot H, Noll T. Enzymic determination of inorganic phosphates, organic phosphates and phosphate-liberating enzymes by use of nucleoside phosphorylase-xanthine oxidase (dehydrogenase)-coupled reactions. Biochem J. 1985; 230:255–260. [PubMed: 2996493]

39. Klenow H. The enzymic oxidation and assay of adenine. Biochem J. 1952; 50:404–407. [PubMed: 14915965]

40. Pflugrath JW. The finer things in X-ray diffraction data collection. Acta Crystallogr D. 1999; 55:1718–1725. [PubMed: 10531521]

41. Schneider TR, Sheldrick GM. Substructure solution with SHELXD. Acta Crystallogr D. 2002; 58:1772–1779. [PubMed: 12351820]

42. Terwilliger TC. Maximum-likelihood density modification. Acta Crystallogr D. 2000; 56:965–972. [PubMed: 10944333]

43. Terwilliger TC. Automated main-chain model building by template matching and iterative fragment extension. Acta Crystallogr D. 2003; 59:38–44. [PubMed: 12499537]

44. Emsley P, Cowtan K. COOT: model-building tools for molecular graphics. Acta Crystallogr D. 2004; 60:2126–2132. [PubMed: 15572765]

45. Read RJ. Pushing the boundaries of molecular replacement with maximum likelihood. Acta Crystallogr D. 2001; 57:1373–1382. [PubMed: 11567148]

46. Murshudov GN, Vagin AA, Dodson EJ. Refinement of macromolecular structures by the maximum-likelihood method. Acta Crystallogr D. 1997; 53:240–255. [PubMed: 15299926]

47. Lamzin VS, Wilson KS. Automated refinement of protein models. Acta Crystallogr D. 1993; 49:129–147. [PubMed: 15299554]

48. Perrakis A, Sixma TK, Wilson KS, Lamzin VS. wARP: improvement and extension of crystallographic phases by weighted averaging of multiple-refined dummy atomic models. Acta Crystallogr D. 1997; 53:448–455. [PubMed: 15299911]

49. Adams PD, Grosse-Kunstleve RW, Hung LW, Ioerger TR, McCoy AJ, Moriarty NW, et al. PHENIX: building newssoftware for automated crystallographic structure determination. Acta Crystallogr D. 2002; 58:1948–1954. [PubMed: 12393927]

50. Kleywegt GJ, Jones TA. Detection, delineation, measurement and display of cavities in macromolecular structures. Acta Crystallogr D. 1994; 50:178–185. [PubMed: 15299456]

51. Schwede T, Kopp J, Guex N, Peitsch MC. SWISS-MODEL: an automated protein homology-modeling server. Nucleic Acids Res. 2003; 31:3381–3385. [PubMed: 12824332]

52. Altschul SF, Gish W, Miller W, Myers EW, Lipman DJ. Basic local alignment search tool. J Mol Biol. 1990; 215:403–410. [PubMed: 2231712]

53. Altschul SF, Madden TL, Schaffer AA, Zhang J, Zhang Z, Miller W, Lipman DJ. Gapped BLAST and PSI-BLAST: a new generation of protein database search programs. Nucleic Acids Res. 1997; 25:3389–3402. [PubMed: 9254694]

54. Gasteiger E, Gattiker A, Hoogland C, Ivanyi I, Appel RD, Bairoch A. ExPASy: The proteomics server for in-depth protein knowledge and analysis. Nucleic Acids Res. 2003; 31:3784–3788. [PubMed: 12824418]

55. Thompson JD, Higgins DG, Gibson TJ. CLUSTALW: improving the sensitivity of progressive multiple sequence alignment through sequence weighting, position-specific gap penalties and weight matrix choice. Nucleic Acids Res. 1994; 22:4673–4680. [PubMed: 7984417]

56. Kabsch W, Sander C. Dictionary of protein secondary structure: pattern recognition of hydrogen-bonded and geometrical features. Biopolymers. 1983; 22:2577–2637. [PubMed: 6667333]

57. Lee JE, Cornell KA, Riscoe MK, Howell PL. Structure of E. coli 5′-methylthioadenosine/S-adenosylhomocysteine nucleosidase reveals similarity to the purine nucleoside phosphorylases. Structure. 2001; 9:941–953. [PubMed: 11591349]

58. Gouet P, Courcelle E, Stuart DI, Metoz F. ESPript: analysis of multiple sequence alignments in PostScript. Bioinformatics. 1999; 15:305–308. [PubMed: 10320398]
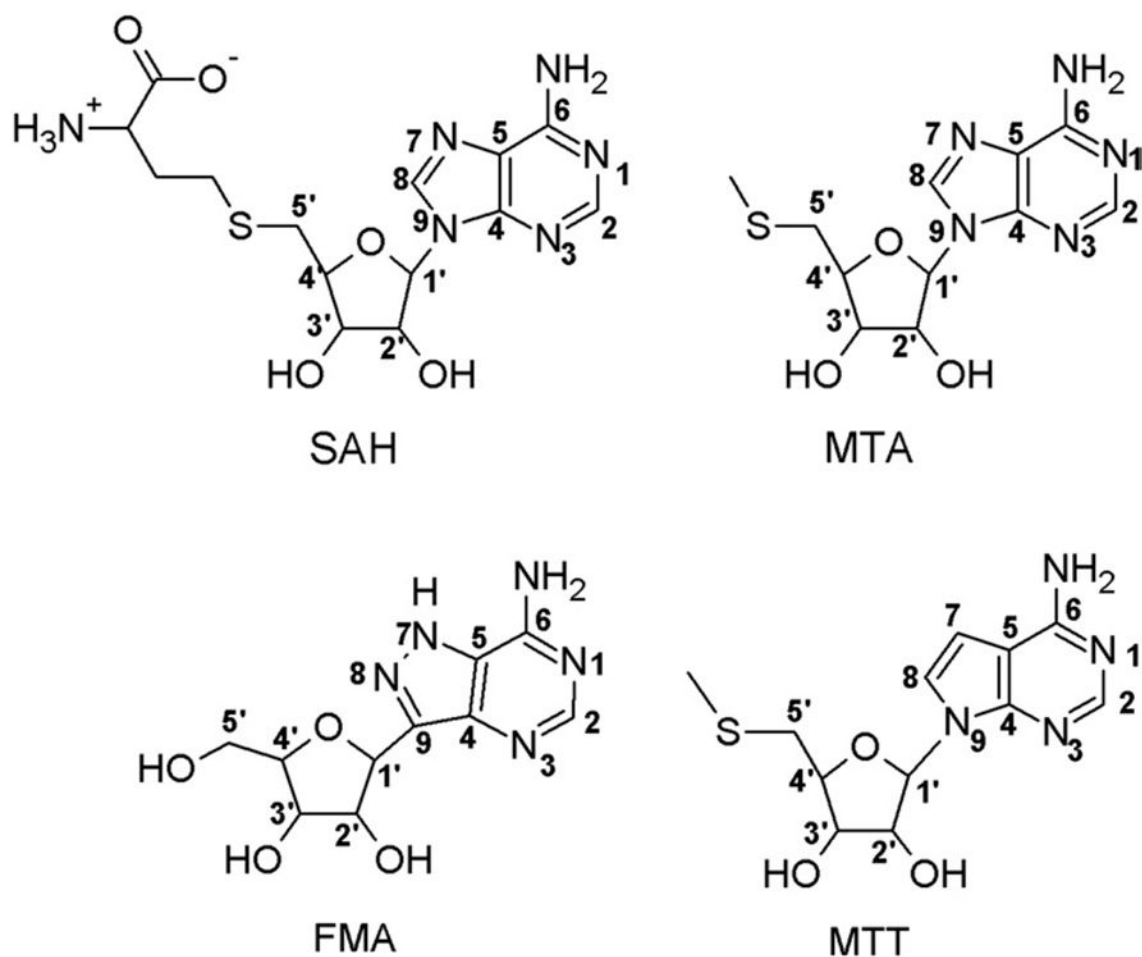
Fig. 1.
The structures of *S*-adenosylhomocysteine (SAH), 5′-methylthioadenosine (MTA), formycin A (FMA), 5′-methylthiotubercidin (MTT). For ease of comparison, the structures are numbered according to MTA rather than the IUPAC convention.
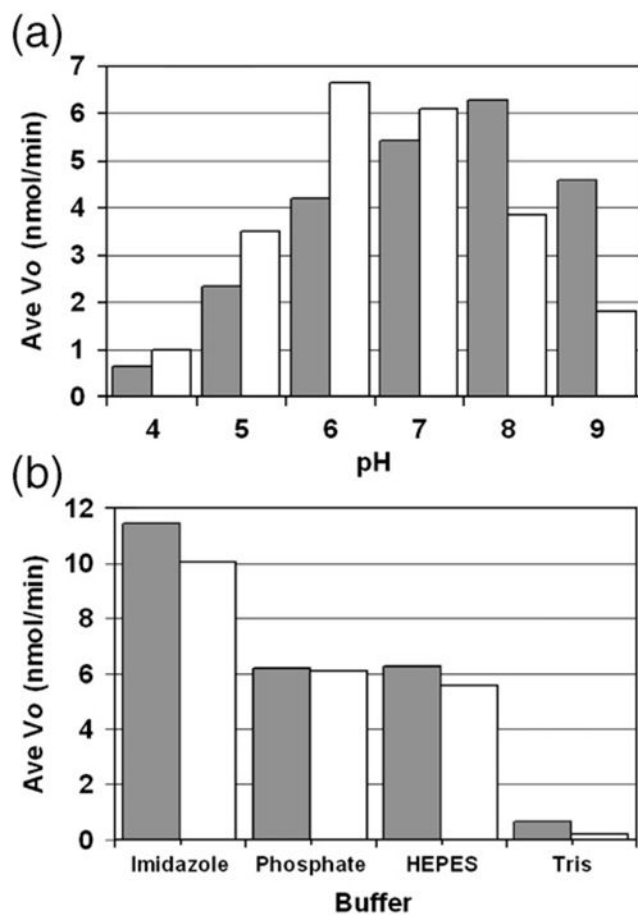
Fig. 2.
Effect of pH and buffer on MTA nucleosidase activity. (a) Effect of pH on MTA nucleosidase activity. Assays were conducted as described in Materials and Methods using 100 mM sodium phosphate (pH 4–9). (b) Buffer effects on MTA nucleosidase activity. All buffers were tested at a concentration of 100 mM at pH 7. *At*MTAN1, gray bars; *At*MTAN2; white bars.
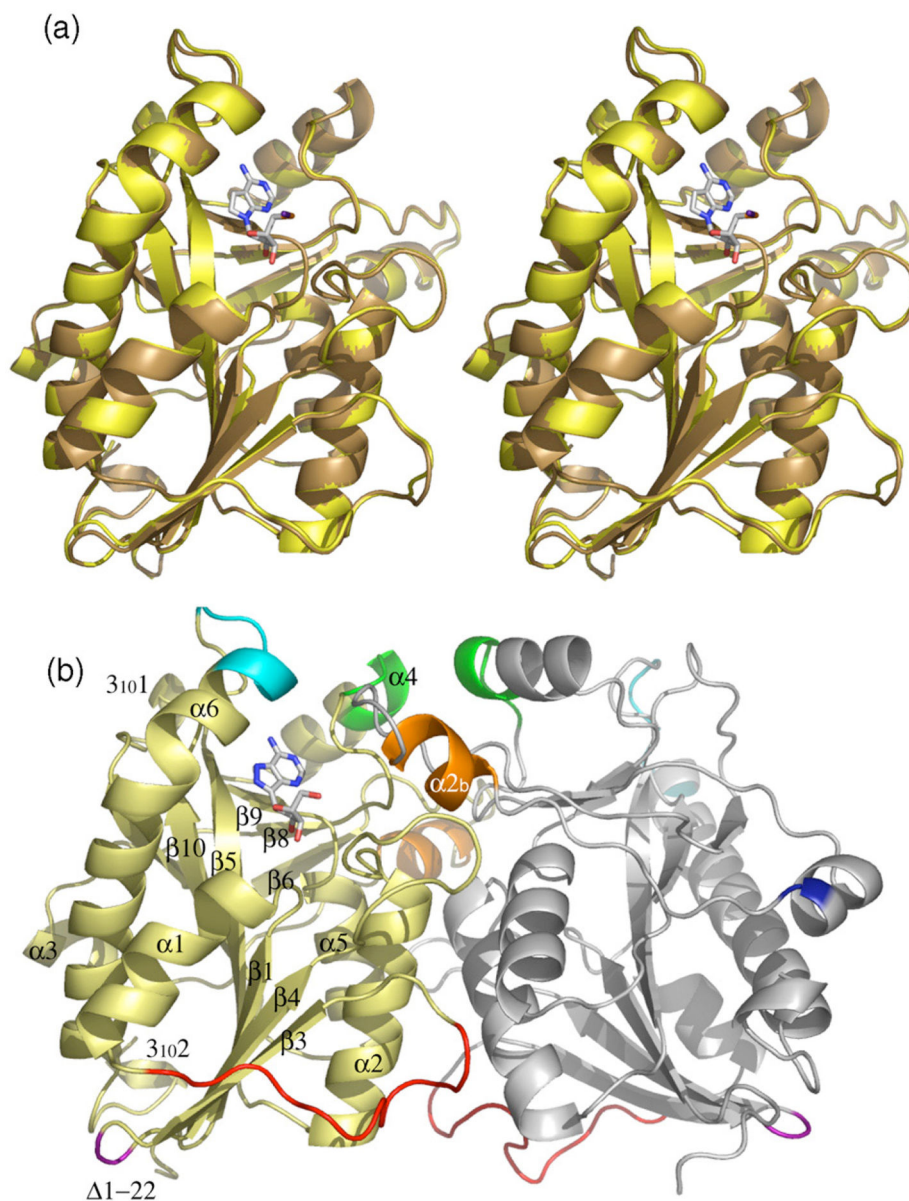
Fig. 3.
Tertiary and quaternary structure of *At*MTAN1. (a) A stereo diagram of the monomer structure of *At*MTAN1. The structures of *At*MTAN1-MTT (brown) and apo-*At*MTAN1 (gold) were aligned using PROFIT. The secondary structure elements were assigned using DSSP.[56] (b) The quaternary structure of *At*MTAN1-FMA. Six regions in *At*MTAN1 that show C^α displacements of >5 Å when aligned with *Ec*MTAN are highlighted as follows: the β2-β3 (red), β3-β4 (purple), α3 (dark blue) and β10-α6 loops (cyan), and the α2b (orange) and α4 (green) helices. This figure, and Figs. 5 and 7 were prepared using PYMOL [http://pymol.sourceforge.net/].
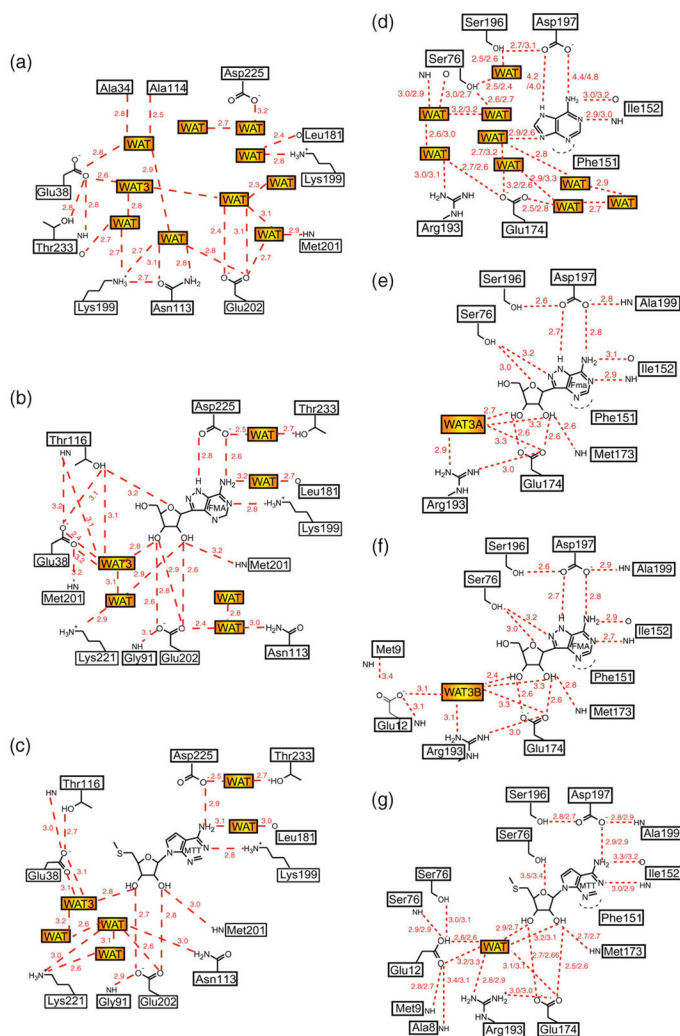
Fig. 4.
A diagram of the interactions in the adenine- and ribose-binding subsites of apo-*At*MTAN1
(a), *At*MTAN1-FMA (b), *At*MTAN1-MTT (c), *Ec*MTAN-ADE (d), *Ec*MTAN-FMA, subunit
A (e), *Ec*MTAN-FMA, subunit B (f) and *Ec*MTAN-MTT (g). Dotted lines represent
hydrogen bond interactions with distances given in Å. Base-stacking interactions are
represented as dotted curves. (d and g) The first and second values correspond to distances
from monomers A and B, respectively. (e–g) adapted from Ref. 57.
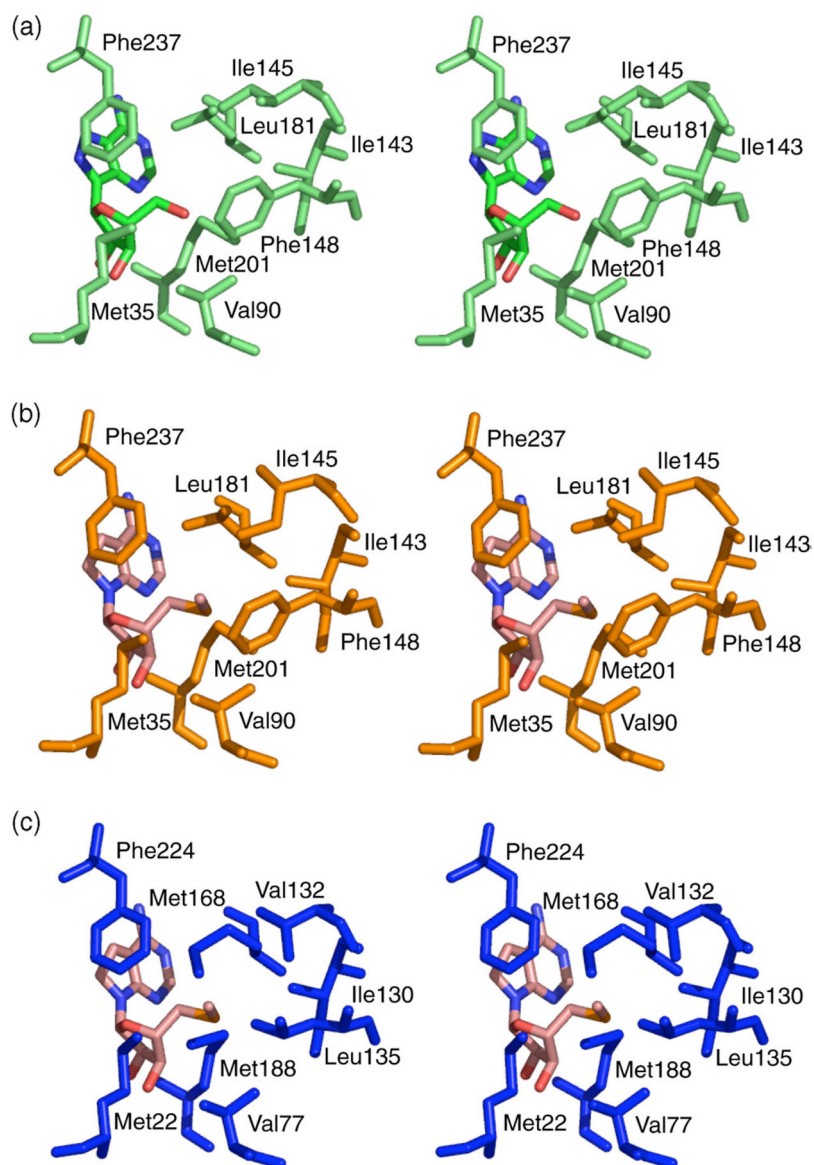
Fig. 5.
The 5′-alkylthio binding subsites in the crystal structures of *At*MTAN1-FMA (a) and *At*MTAN1-MTT (b), and the homology model of *At*MTAN2 (c). MTT was modeled into the *At*MTAN2 active site for comparison purposes.
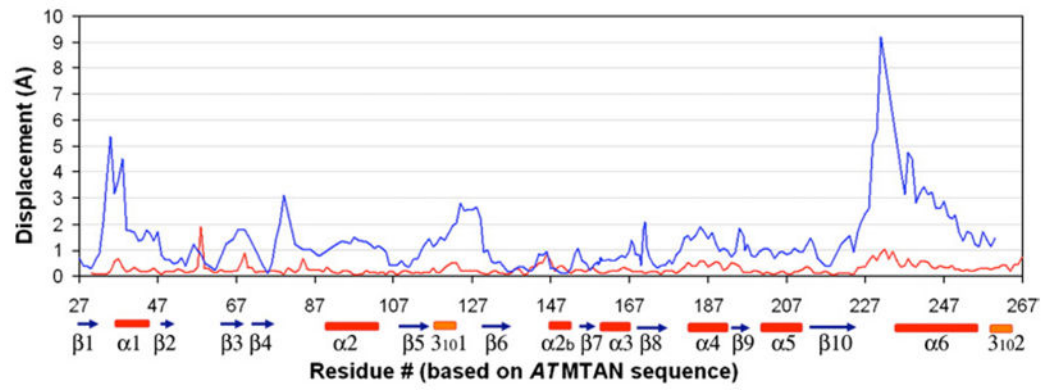
Fig. 6.
A plot of the displacements in C$^\alpha$ positions between the MTT-bound and open forms of
*Ec*MTAN (blue), and of *At*MTAN1 (red). The topology of *At*MTAN1 is illustrated below
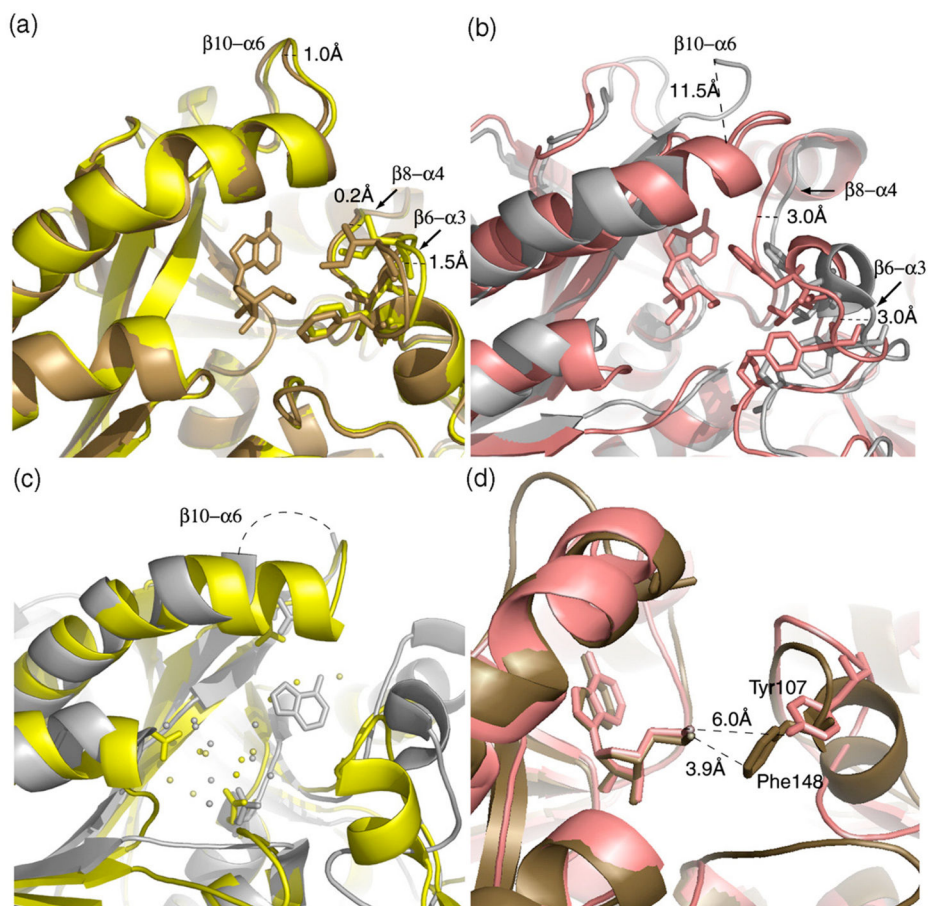the *x*-axis.

Fig. 7.
Conformational changes in the active sites of *At*MTAN1 (a) and *Ec*MTAN (b) upon binding of FMA or MTT. (c) Superimposition of *Ec*MTAN-Ade and apo-*At*MTAN1. Electron density is missing for the β10-α6 loop in *Ec*MTAN because of disorder, so this region is not modeled in the structure and is represented here by a dotted line. (d) Superimposition of *Ec*MTAN-MTT and *At*MTAN1-MTT highlighting the positions of Phe148 in *At*MTAN1 and Tyr107 in *Ec*MTAN and their relative proximities to the 5′-alkylthio end of the ligand. In all panels, the *apo*- and MTT-bound structures of *At*MTAN1 are shown in yellow and brown, respectively, while the ADE- and MTT-bound forms of *Ec*MTAN are shown in gray and pink, respectively.
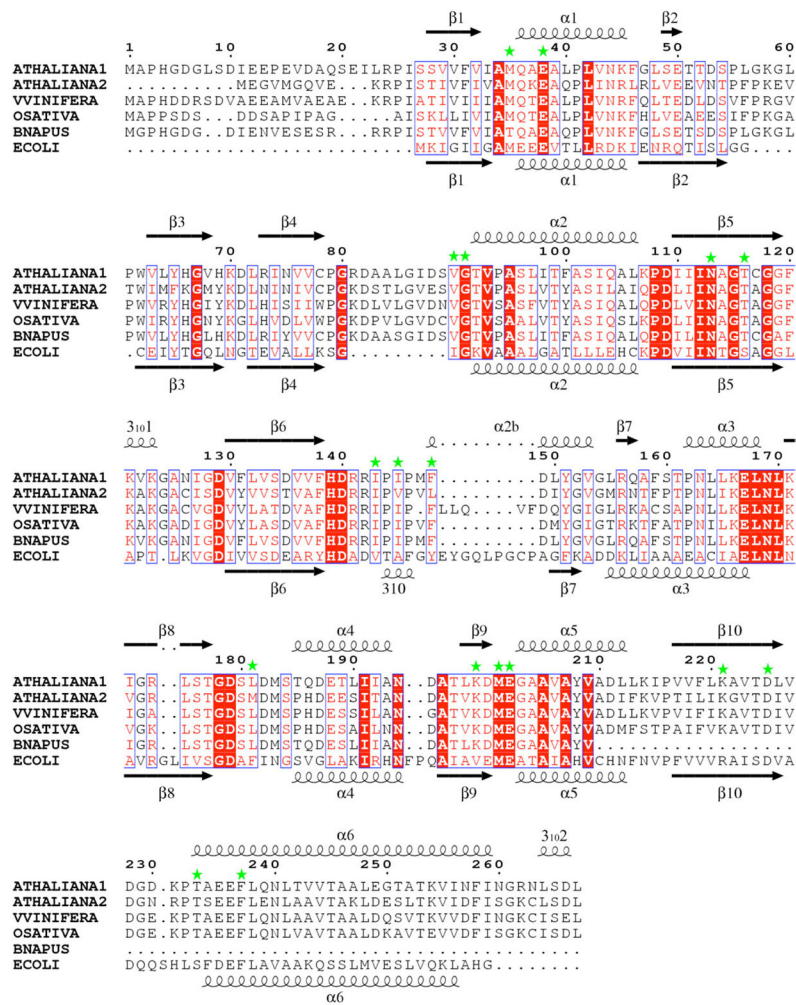
Fig. 8.
Sequence alignment of plant MTANs from *A. thaliana, V. vinifera, O. sativa* and *B. napus.*
ATHALIANA1 and ATHALIANA2 refer to *At*MTAN1 and *At*MTAN2 homologues from *A. thaliana.* Please note that the *B. napus* MTAN sequence is translated from an EST sequence and may be incomplete. The sequence of *E. coli* MTAN is included for comparison purposes. The structural topologies at the top and bottom of the blocks correspond to *At*MTAN1 and *Ec*MTAN, respectively. Residues that are strictly conserved a white character in a red box, while residues that have been conservatively substituted are are shown as red characters. Residues that are similar across groups are framed in blue. Residues involved in ligand binding are marked with green asterisks. The figure was prepared using ESPript.[58]

Table 1

Catalytic activity and substrate specificity of *At*MTAN1 and *At*MTAN2

	*At*MTAN1			*At*MTAN2		
Substrate	**5′-Methylthioadenosine (MTA)**			**5′-Methylthioadenosine (MTA)**		
K_m (µM)	7.1±0.5			3.4±0.2		
V_{max} (nmol/min)	3.7±0.1			2.0±0.08		
k_{cat} (s^{-1})	18.7			2.0		
k_{cat}/K_m (s^{-1} $µM^{-1}$)	2.6			0.6		
Substrate	Ave rel. velocity±S.D. (A_{275}/min)	Specific activity (U/mg)	% Max activity	Ave rel. velocity±S.D. (A_{275}/min)	Specific activity (U/mg)	% Max activity
5′-Methylthioadenosine (MTA)	0.0530±0.0031	11.05	100	0.0100±0.0007	6.25	100
5′-Ethylthioadenosine (ETA)	0.0212±0.0020	4.42	40	0.0042±0.0002	2.60	42
5′-Isobutylthioadenosine (IBTA)	0.0089±0.0007	1.85	17	0.0032±0.0004	1.98	32
5′-Butylthioadenosine (BTA)	0.0131±0.0002	2.72	25	0.0024±0.0008	1.50	24
5′-Phenylthioadenosine (PhTA)	0.0065±0.0009	1.36	12	0.0039±0.0002	2.44	39
S-Adenosylhomocysteine (SAH)	0.0000	0.0	0	0.0014±0.0006	0.9	14
Adenosine (ADO)	0.0000	0.0	0	0.0006±0.0001	0.38	6
5′-Choroadenosine (ClADO)	0.0022±0.0003	0.46	4	0.0013±0.0004	0.83	13
5′-Iodoadenosine (IADO)	0.0151±0.0011	3.14	28	0.0017±0.0002	1.06	17

Table 2

Diffraction Data and MAD Phasing statistics

Se-Met-*At*MTAN1-FMA	Peak	Inflection	Remote
Space Group		$P2_1$	
Cell dimensions			
a (Å)		46.0	
b (Å)		126.6	
c (Å)		83.6	
β (deg.)		102.1	
Wavelength (Å)	0.9794	0.9796	0.95
Total no. reflections	721061	361971	261457
No. unique reflection	140545	129318	89939
Average redundancy[a]	4.9	2.6	2.8
Resolution range (Å)[b]	45.0–1.9 (2.0–1.9)	45.0–1.9 (2.1–1.9)	45.0–2.2 (2.3–2.2)
R_{merge}[c] (%)[b]	7.0 (22.0)	6.7 (22.0)	7.1 (20.0)
Completeness (%)[b]	96.3 (97.3)	93.7 (96.6)	95.2 (94.2)
$<I>/\sigma I$[b]	11.6 (6.3)	8.2 (4.1)	8.6 (4.8)
Figure of merit (FOM)	0.47		
FOM after solvent flipping	0.67		

	*At*MTAN1	*At*MTAN1-FMA	*At*MTAN1-MTT
Space group	$P2_1$	$P2_1$	$P2_1$
Cell dimensions			
a (Å)	41.3	40.3	40.6
b (Å)	127.1	126.9	126.1
c (Å)	45.5	45.3	45.5
β (deg.)	109.6	106.8	109.0
Wavelength (Å)	1.542	1.542	1.542
Total no. reflections	91,173	99,304	293,556
No. unique reflection	28,189	31,340	35,692
Average redundancy	3.2	3.1	8.2
Resolution range[b] (Å)	23.2–2.0 (2.1–2.0)	23.6–1.9 (2.0–1.9)	32.7–1.8 (1.9–1.8)
R_{merge}[c] (%)[b]	8.1 (26.0)	6.0 (16.0)	5.6 (29.0)
Completeness (%)[b]	94.6 (90.7)	94.8 (90.5)	95.7 (97.5)
$<I>/\sigma I$[b]	8.9 (4.0)	12.6 (5.2)	19.7 (6.8)

[a]Only the symmetry-equivalents are merged for Se-Met *At*MTAN1-FMA MAD data.

[b]Values in parentheses correspond to the value in the highest resolution shell.

[c]$R_{merge}= \Sigma\Sigma|I(k)-<I>|/\Sigma\Sigma\ I(k)$ where $I(k)$ and $<I>$ represent the diffraction intensity values of the individual measurements and the corresponding mean values.

Table 3

Refinement statistics

	*At*MTAN1	*At*MTAN1-FMA	*At*MTAN1-MTT
Resolution range (Å)	23.2–2.0	23.6–1.9	32.7–1.8
No. reflections in refinement	25313	33094	32153
No. reflections in test set	2531	3309	3215
Total no. non-hydrogen atoms	3984	4212	4075
No. protein atoms	3715	3730	3672
No. ligand atoms	0	38	40
Occupancy of inhibitor			
Monomer A	\	0.0	1.0
Monomer B	\	0.69	1.0
Number of water molecules	249	441	358
R (%)[a]	19.8	17.2	18.5
R_{free} (%)[a]	25.4	23.3	18.9
rmsd from ideal geometry			
Bond lengths (Å)	0.015	0.014	0.018
Bond angles (deg.)	1.5	1.6	1.8
Dihedral angles (deg.)	25.1	24.3	24.8
Improper angles (deg.)	4.8	4.3	5.4
Cruickshank's DPI based on R_{free}[b]	0.21	0.18	0.13
Average B-factor			
Overall (Å^2)	27.2	19.3	22.8
Chain A (Å^2)	28.0	19.9	22.7
Chain B (Å^2)	27.5	17.2	21.3
Inhibitor (Å^2)	\	15.9	18.8
Ramachandran plot[c]			
Most favoured (%)	90.3	92.7	91.7
Allowed (%)	9.0	6.6	7.3
Generously allowed (%)	0.7	0.7	0.9
Disallowed (%)	0	0	0
Correlation coefficient (F_o–F_c)	0.95	0.96	0.96
Correlation coefficient (F_o–F_c) free	0.92	0.93	0.96
FOM after refinement[d]	0.80	0.85	0.91

[a] $R_{\text{cryst}} = \Sigma |F_{\text{obs}} - F_{\text{calc}}| / \Sigma |F_{\text{obs}}|$; R_{free} is R_{cryst} for the 10% cross validated test data.

[b] Cruickshank's diffraction component precision index (DPI) as an estimate of coordinate error.[53]

[c] Ramachandran analysis by PROCHECK.[54]

[d] FOM=$1-m$, where $m=[(\cos \phi)^2 - (\sin \phi)^2]^{1/2}$.